Supplementary information for : Pulsed-laser induced gold microparticle fragmentation by thermal strain

By Yogesh Pokhrel, Meike Tack, Sven Reichenberger, Matteo Levantino, and Anton Plech

1. Experimental details

Microparticle irradiation

The gold microparticle powder with quasi-spherical particles and a narrow size distribution close to 1.2 µm in diameter was purchased from Evochem and suspended in water by ultrasonic agitation. Scanning electron microscopy (SEM) images of the powder are displayed in fig. 1 a. The particles settle within a ten-minute time scale but can easily be resuspended by shaking. A suspension (400 mg/l) was loaded into a polyethylene syringe that contained a magnetic stirrer bar to counter sedimentation. A syringe pump injects the suspension at a rate of 3.2 ml/min into an open-ended glass capillary (0.3 mm diameter, Hilgenberg). A free round jet is formed that is irradiated from the side by 1 ps laser pulses at 400 nm from a regenerative amplifier laser system (Coherent) at the beamline ID09 at the European Synchrotron Radiation Facility (Grenoble, France). Coaxially to the direction of the focused laser beam (0.24 mm full width at half maximum), a pulsed x-ray beam probes the structure of the sample at the same repetition rate of 1 kHz. The laser fluence can be considered to be quite homogeneous within the probed area of the x-ray beam (0.04 mm) with an estimated 20 % variation. The liquid was collected after irradiation at an incident fluence of 2700 J/m2 and analyzed via SEM and transmission electron microscopy (TEM). For this analysis, the fragments are stabilized by 0.5 M NaOH at pH 10. Note that irradiated particles in the collected liquid are much less abundant than non-irradiated ones because of the difference in laser spot and jet size. Therefore, the size distributions and concentrations found in the TEM analysis are not representative of the *in situ* abundance of fragmentation products.

Analysis of the scattering signal

The scattered x-rays are recorded on a 2D area detector (Rayonix HS170), whose distance from the sample can be varied to cover a scattering vector $q=4\cdot\pi/\lambda \cdot \sin(2\Theta/2)$ from 0.01 to 5 $Å^{-1}$, with λ and 2Θ being the x-ray wavelength and full scattering angle, respectively. The x-ray signal has rotational symmetry with respect to the incoming x-ray beam due to the averaging over all orientations of the microparticles. In standard processing of background subtraction, space angle correction, a one-dimensional scattering distribution I(q) is derived. In practice, two sets of data are recorded, one with the x-ray pulses arriving 2 nanoseconds before the laser pulses ("negative delay") and one with the x-ray pulses following the laser pulses by a de- fined delay to probe the time

dependence of the dynamics. A difference ΔI(q) of the two signals contains only a signal pertaining to laser-induced structural changes in the sample. The observables deduced from this signal have been discussed in detail earlier [15,16]. In brief, the gold (111) powder peak can be analyzed in position, amplitude, and width to conclude on particle heating, melting and strain formation. Liquid scattering can provide information on the thermodynamic state of water. The full x-ray scattering intensity S(q) in a q range between 0.2 and 4.3 $Å^{-1}$ is shown in fig. 1b) together with the contribution from gold powder scattering, as well as a difference scattering curve at a delay of 45 ps and fluence of 2700 J/m^2. Note the different amplitudes of the full scattering and the powder scattering of gold, the latter amounting only to 7 % of the water background. Small angle scattering finally reflects all changes in large-scale structure from few nm to about 60 nm in the present case. Previously, we have derived changes of particle sizes and shapes of irradiated initial nanoparticles [16,30] as well as the quantification of the formation of vapor bubbles by cavitation [31,32].

However, compared to the q-values that indicate shape changes (Guinier range close to $q_{Guinier} \simeq \pi/R$ with R being the characteristic length scale or the radius), the microparticles scatter at q-values that were below the accessible detection range of the standard pinhole detector setup used in this study ((lower limit 0.009 $Å^{-1}$, which practically allows one to resolve particles of < 50 nm in diameter)). Small-angle scattering for compact particles generally decays with a power law of $S(q) \propto K\, q^{-4}$ for q larger than the Guinier range independent of the actual radius values and can therefore be detected in the accessible q window. The proportionality K can be used to express the total specific surface area A [33,34]:

$$A = K/ (2\pi r_e^2 \ (N_A \cdot Z/(M \cdot \Delta\rho_{p-l})))$$

with the scattering cross section expressed by the classical electron radius re, Avogadro's constant N_A, atomic number Z, molecular mass M and electron density contrast $\Delta\rho_{p-l}$ between particle p and liquid l. Thus, the amplitude of the SAXS signal is proportional to the total surface area of the particles. The derivation of the amplitude is conveniently performed by averaging the experimental SAXS signal over a finite q range q_P that obeys the Porod law. We chose the interval between 0.014 and 0.056 $Å^{-1}$ to extract $\Delta I(q_P)$.

Simulation of the heat flow in microparticles

Laser excitation and heat flow through the microparticles is simulated by using a numerical code for evaluating laser penetration, coupling to electrons and phonons (two-temperature model, TTM) and diffusional transport of hot electrons and phonons through the particle. The Python code NTMPy [35] is freely available (https://github.com/udcm-su/NTMpy) and codes this transport in thin films using an optional tilted incidence angle for the laser. The fluence input value therefore assumes the incident laser fluence, not only the part absorbed in the particle. Here, a sphere of

0.6 µm radius has been divided into 12 equal annular regions (linearly progressing radius) n of fixed incidence angle and thickness (see fig S1). The latter was chosen with respect to the thickness of the sphere at a given radius from the rotation axis parallel to the propagation of the plane-wave laser light. The gold layer is sandwiched between two water layers of each 300 nm thickness that are transparent to the laser but accept heat through transfer across the interface. This approach is limited by neglecting polarization effects and not allowing for transverse heat flow (perpendicular to the annual slices). On the other hand, the transport of both electrons and phonons is correctly described, which matters for gold with a particularly long electron-phonon time and important electron transport [36,37]. The assembly of these independently simulated slices produces the spatiotemporal distribution of heat in a photo-excited gold sphere, as shown in fig. 2. For visual support, these 12 slices have been interpolated to 36 raster lines in the y dimension.

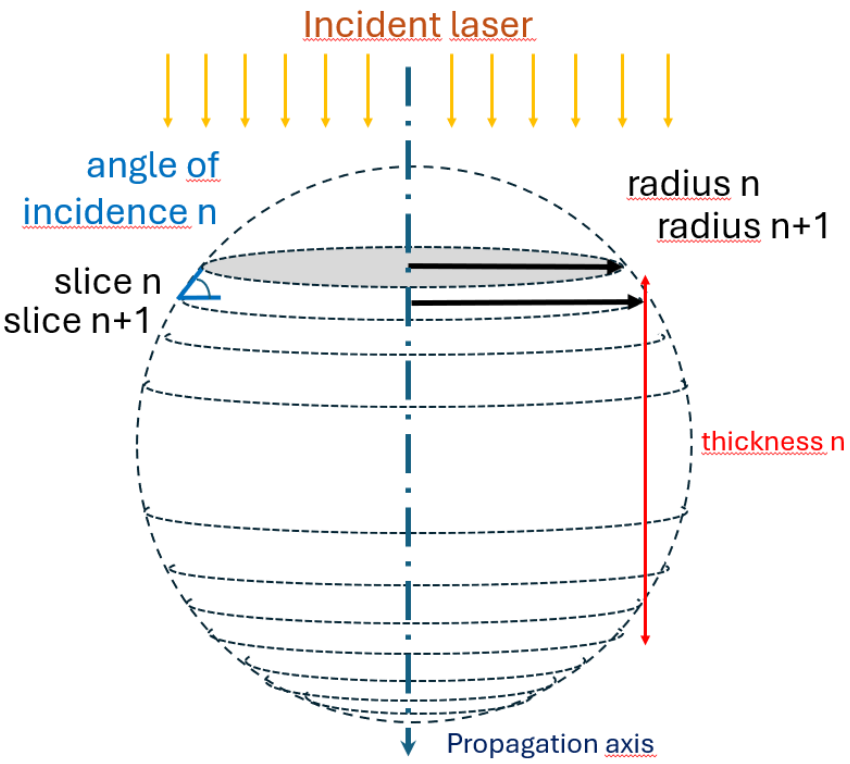

Fig. S1: Division of sphere into 12 annular cylinders of progressing radius with given thickness and angle of incidence of each segment as function of radius for laser light propagation from the top.

1. Additional data on electron and phonon temperature of the TTM simulations

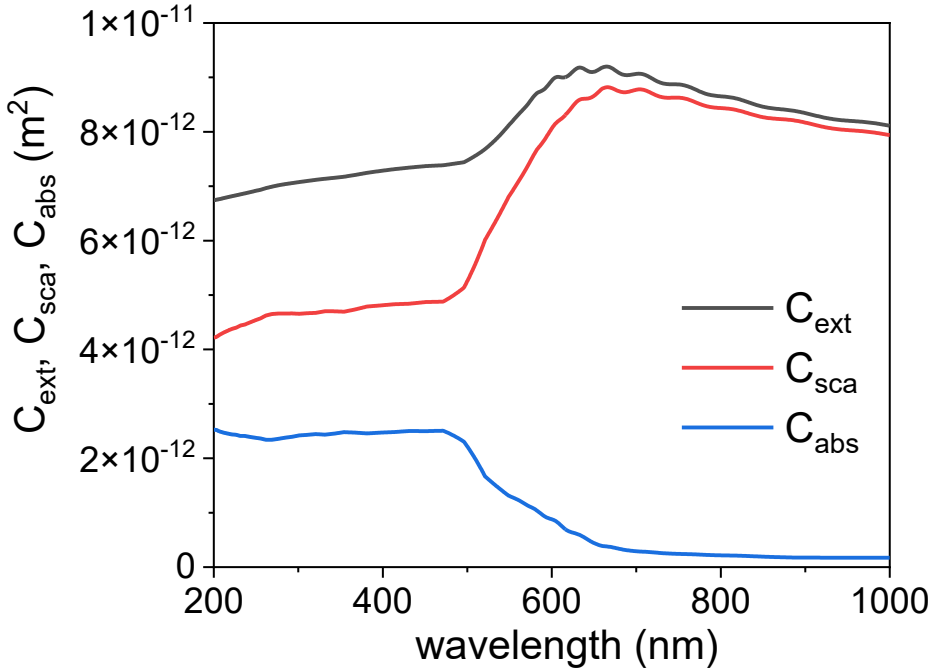

Fig. S2: Extinction cross section (C_{ext}), absorption cross section (C_{abs}), and scattering cross section (C_{sca}), of a gold microparticles of 1.2 µm diameter in water (optical constants gold: P B Johnson& R W Christy, Phys Rev B 6 4370-4379 (1972), water: D. J. Segelstein. *The complex refractive index of water*, Master Thesis (1981)) as function of wavelength with absorption amounting for 34 % of total extinction according to Mie theory as computed by [41].

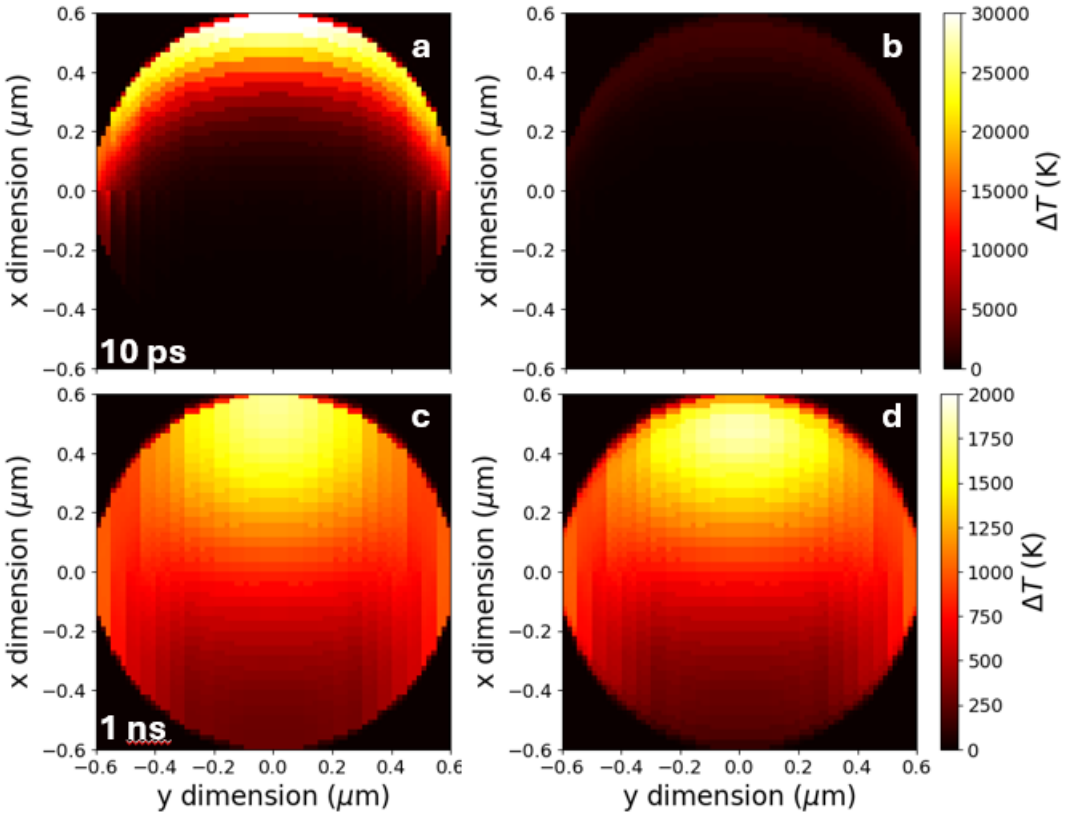

Fig. S3: Distribution of temperature rise after given delays of 10 ps and 1 ns for the electronic temperature (a, c) and phonon temperature across the microparticle section. Note the change in temperature scale from a and b to c and d.

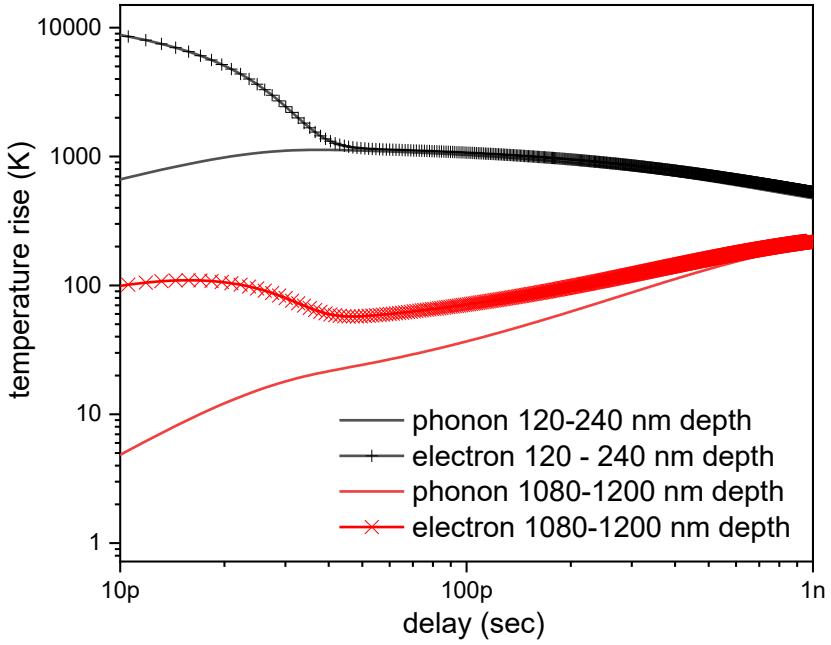

Fig. S4: Course of electronic and phonon temperatures as function of delay at the front of the particle (120 – 240 nm) and the back of the particle (1080-1200 nm) on the propagation axis.

2. Additional simulational data on the water temperature rise

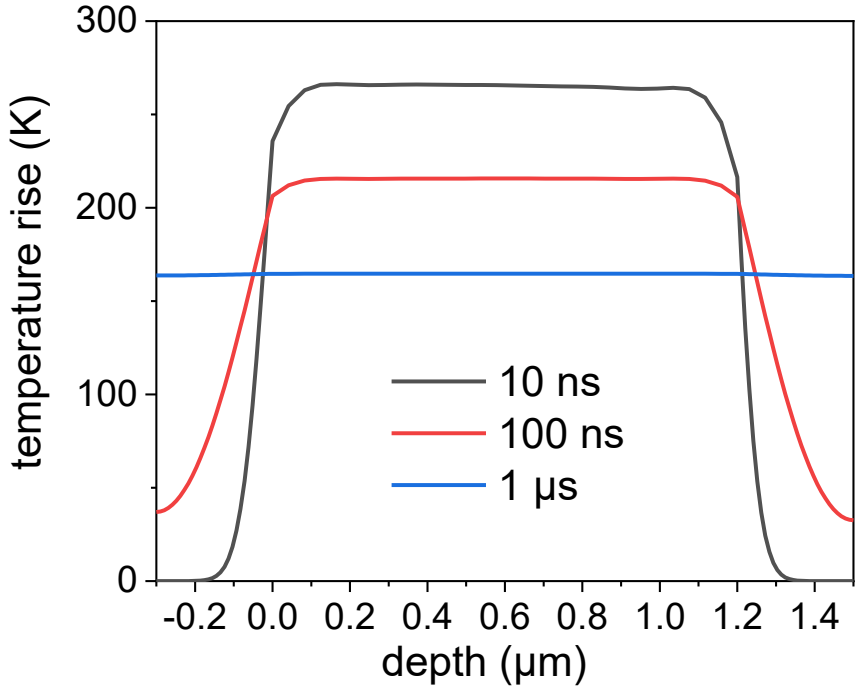

Fig. S5: Temperature profile across the microparticle on the propagation axis at several delays. Note that the water-particle interface is located at 0 and 1.2 μm.

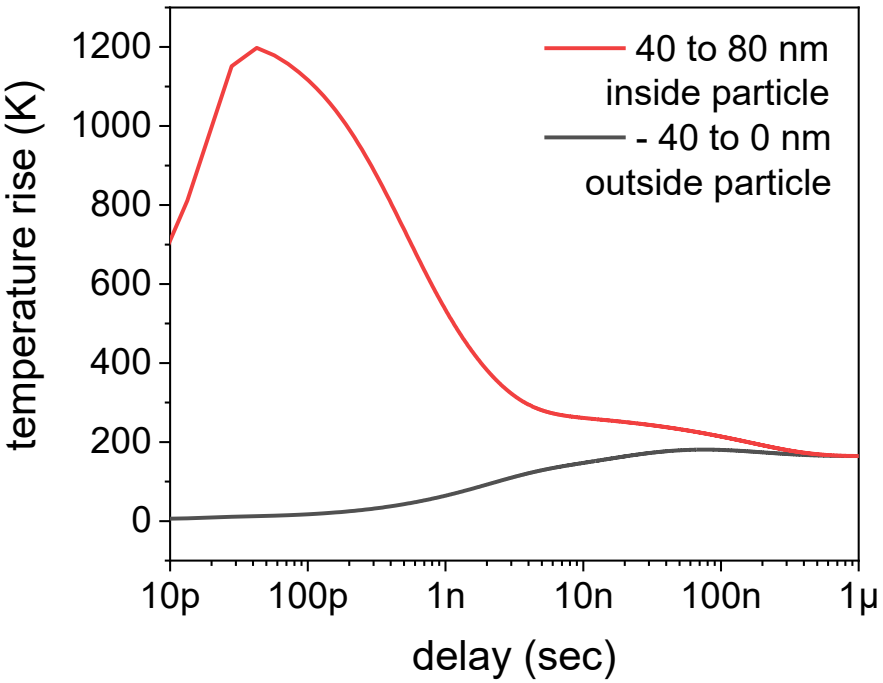

Fig S6: Temperature change in the vicinity of the front surface of the microparticle to water from the TTM simulations at 85 J/m^2. The temperature in water rises by 180 K at a 100 ns delay, before equilibrating with the still heated microparticle.